# Zn$_{1-x}$Cd$_x$S Solid Solutions with Controlled Bandgap and Enhanced Visible-Light Photocatalytic H$_2$-Production Activity

Qin Li,[†] Huan Meng,[†] Peng Zhou,[†] Yingqiu Zheng,[†] Juan Wang,[†] Jiaguo Yu,[†,*] and JianRu Gong[‡,*]

[†]State Key Laboratory of Advanced Technology for Materials Synthesis and Processing, Wuhan University of Technology, Wuhan 430070, People's Republic of China

[‡]National Center for Nanoscience and Technology, 11 Zhongguancun Beiyitiao, Beijing 100190, People's Republic of China

ABSTRACT: Photocatalytic hydrogen (H$_2$) production from water splitting under visible-light irradiation is considered to be an attractive way to solve the increasing global energy crises in modern life. In this study, highly efficient photocatalytic H$_2$ production without the assistant of a cocatalyst was achieved using Zn1$_{1-x}$Cd$_x$S solid solutions as the visible-light-driven photocatalysts and a mixed Na$_2$S and Na$_2$SO$_3$ aqueous solution as the sacrificial reagent. The Zn$_{1-x}$Cd$_x$S samples were prepared by a simple zinc–cadmium–thiourea (Zn–Cd–Tu) complex thermolysis method using thiourea, zinc acetate (Zn(Ac)$_2$), and cadmium acetate (Cd(Ac)$_2$) as the precursors. The obtained Zn$_{1-x}$Cd$_x$S solid solutions feature a small crystallite size and precisely controllable band structure, which are beneficial for the photocatalysis. When the Zn/Cd molar ratio is 1:1, the

prepared Zn$_{0.5}$Cd$_{0.5}$S sample exhibits the highest H$_2$-production rate of 7.42 mmol·h^{-1}·g^{-1}, exceeding that of the pure CdS and ZnS samples by more than 24 and 54 times, respectively, and even much higher than that of the optimal Pt-loaded CdS. This high photocatalytic H$_2$-production activity is attributed predominantly to enough visible-light absorption capacity and suitable conduction band potential of the Zn$_{0.5}$Cd$_{0.5}$S solid solution, which is further evidenced from the related theory calculations on the band structures of the Zn$_{1-x}$Cd$_x$S solid solutions. Moreover, the calculation on the Mulliken populations of Zn, Cd, and S atoms for the first time provides new insight into the deep understanding of the chemical shifts of element binding energies for the Zn$_{1-x}$Cd$_x$S solid solutions and the designing of new ternary photocatalytic materials.
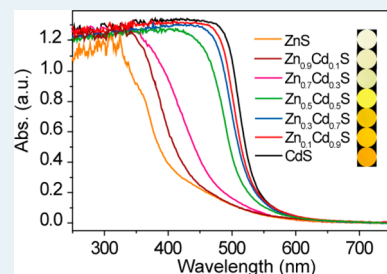
KEYWORDS: Zn$_{1-x}$Cd$_x$S solid solution, thermolysis, theory calculation, visible light, hydrogen production

1. INTRODUCTION

Considering the increasing global energy crises and serious environmental pollution caused by the burning of fossil fuels, capturing freely available solar energy and converting it into hydrogen (H$_2$) energy has received much attention because H$_2$ is an ideal candidate for the replacement of fossil fuels in the future for its recycling possibility and environmental friendliness.[1,2] Since the first report on photocatalytic splitting of water on TiO$_2$ electrodes was published in 1972 by Honda and Fujishima,[3] H$_2$ production from water splitting using semiconductors as photocatalysts under solar-light irradiation has been proven to be an ideal route for the efficient conversion of solar energy into chemical energy.[4–9] However, TiO$_2$ has no visible-light response due to its large band gap of 3.2 eV.[10] Recently, much research has been focused on the development of visible-light-responsive photocatalysts to take advantage of the solar light resources more effectively because visible light constitutes a larger proportion than UV light in solar light. In fact, metal chalcogenides due to appropriate band gap width and band edge position have elicited more and more attention in photocatalytic H$_2$ production.[11] Especially, CdS has been proven to be an efficient semiconductor H$_2$-production photocatalyst and has been extensively studied.[12] However, some problems, such as quick recombination of photogenerated charge carriers and photocorrosion under visible-light irradiation, still exist and prohibit the wide application of

CdS to a large extent. To solve these problems, forming Zn$_{1-x}$Cd$_x$S solid solutions is regarded as a viable method because ZnS possess the same coordination mode with CdS,[13–15] and the band gap width and band edge position of the Zn$_{1-x}$Cd$_x$S solid solutions can be flexibly tuned by changing the molar ratio of ZnS and CdS.[16,17] Therefore, the synthesis of Zn$_{1-x}$Cd$_x$S solid solutions is of immense technological importance.

To fabricate Zn$_{1-x}$Cd$_x$S solid solutions, numerous methods have been explored, including coprecipitation,[17,18] microemulsion,[19] chemical bath deposition,[20] cation exchange,[13] hydrothermal,[21,22] thermolysis,[23] and so on. For the coprecipitation method, the final element composition of obtained solid solution may not follow the initial stoichiometric ratio due to some metal ions being washed away in the preparation process.[17] For the cation exchange method, it is difficult to obtain band-structure-controlled Zn$_{1-x}$Cd$_x$S solid solutions because the radius of Cd^{2+} (0.97 Å) is much larger than that of Zn^{2+} (0.74 Å).[13] For the hydrothermal method, it always needs a long time to prepare well-crystallized solid solutions.[24] In contrast, for the thermolysis method, the samples heat-treated at high temperatures usually show a high formation rate

Table 1. Experimental Conditions for the Preparation of the $Zn_{1-x}Cd_xS$ (x = 0, 0.1, 0.3, 0.4, 0.5, 0.6, 0.7, 0.9, and 1.0) Samples and Their Physical and Chemical Properties

initial x	final x (ICP-AES)	crystallite size^a (nm)	S_{BET} (m²/g)	av pore size (nm)	band gap		H_2-production rate (mmol·h⁻¹·g⁻¹)
					by KM method (eV)	by DFT (eV)	
0	0	14.0	46.3	10.1	3.10	1.921	0.14
0.1	0.09	12.4	43.0	10.3	3.00	1.664	1.08
0.3	0.32	11.6	34.9	11.2	2.76	1.402	1.42
0.4	0.41	10.9	33.5	13.3	2.57	1.456	3.37
0.5	0.50	10.1	32.9	13.9	2.45	1.356	7.42
0.6	0.59	10.8	30.8	15.8	2.42	1.276	4.45
0.7	0.70	11.9	26.6	17.8	2.35	1.276	1.78
0.9	0.90	13.3	17.0	17.9	2.33	1.180	0.41
1.0	1.00	13.9	16.0	18.0	2.30	1.146	0.31

^{a}Average crystallite size is determined by the broadening of $Zn_{1-x}Cd_xS$ (101) facet diffraction peak using Scherrer equation.

of solid solution in a relatively short time,[23] and the obtained solid solutions show high crystallinity and high photocatalytic activity. For example, Bao et al. reported facile thermolysis synthesis of phase-controlled CdS nanocrystals with enhanced visible-light photocatalytic H_2-production activity.[25] However, to the best of our knowledge, there are no reports on the fabrication of $Zn_{1-x}Cd_xS$ solid solutions by the thermolysis method using thiourea as the S source. In this study, for the first time, we report a simple thermolysis method for the preparation of $Zn_{1-x}Cd_xS$ solid solution nanoparticles (NPs) with enhanced visible-light photocatalytic H_2-production performance. Furthermore, the causes of visible-light absorption and photoactive enhancement for the $Zn_{1-x}Cd_xS$ solid solution were investigated and discussed by considering the changes in energy gaps, distributions of charges, and energies of the band edges. This study will provide new insights into understanding the mechanism of visible-light absorption and photoactive enhancement for $Zn_{1-x}Cd_xS$ solid solution and designing new ternary photocatalytic materials.

2. EXPERIMENTAL SECTION

2.1. Sample Preparation. $Zn_{1-x}Cd_xS$ solid solutions were prepared by a simple zinc−cadmium−thiourea (Zn−Cd−Tu) complex thermolysis method using thiourea (Tu), zinc acetate dihydrate ($Zn(Ac)_2·2H_2O$), and cadmium acetate dihydrate ($Cd(Ac)_2·2H_2O$) as precursors.[25,26] All of the reagents were of analytical grade and were used without further purification. Deionized (DI) water was used in all experiments. In a typical synthesis of the Zn−Cd−Tu complex, given amounts of $Zn(Ac)_2·2H_2O$ and $Cd(Ac)_2·2H_2O$ in different Zn/Cd molar ratios were dissolved in 30 mL of ethanol under constant stirring for 30 min at room temperature. The total amount of $Zn(Ac)_2·2H_2O$ and $Cd(Ac)_2·2H_2O$ was 2.5 mmol. Simultaneously, 10 mmol of thiourea was dissolved in 30 mL of ethanol under constant stirring at 60 °C to form a clear solution. The above two solutions were mixed together under ultrasonic irradiation for 2 h, then the mixed solution was dried in an oven at 80 °C to evaporate the solvent ethanol and obtain the Zn−Cd−Tu complex solid powder. Finally, the dried Zn−Cd−Tu complex powders were calcined in N_2 atmosphere at 500 °C for 30 min to produce the $Zn_{1-x}Cd_xS$ solid solution. The prepared $Zn_{1-x}Cd_xS$ solid solution has a variable composition, where x is 0, 0.1, 0.3, 0.4, 0.5, 0.6, 0.7, 0.9, and 1.0 (see Table 1).

2.2. Characterization. Powder X-ray diffraction (XRD) patterns were obtained on an X-ray diffractometer (Rigaku,

Japan) using Cu Kα irradiation source (λ = 1.54056 Å) at a scan rate of 0.05° 2θ s⁻¹ to determine the crystal phase of the prepared samples. The accelerating voltage and applied current were 40 kV and 80 mA, respectively. The average crystallite size was calculated using the Scherrer equation (d = 0.9λ/B cosθ, where d, λ, B and θ are crystallite size, Cu Kα wavelength (0.154056 nm), full width at half-maximum intensity (fwhm) in radians, and Bragg's diffraction angle, respectively). Transmission electron microscopy (TEM) and high-resolution transmission electron microscopy (HRTEM) images were taken on a JEM-2100F electron microscope (JEOL, Japan) using a 200 kV accelerating voltage. UV−visible diffused reflectance spectra of the samples were obtained for the dry-pressed disk samples on a UV−visible spectrophotometer (UV2550, Shimadzu, Japan). $BaSO_4$ was used as a reflectance standard. The Brunauer−Emmett−Teller (BET) specific surface area (S_{BET}) of the powders was analyzed by nitrogen adsorption in a Micromeritics ASAP 2020 nitrogen adsorption apparatus (USA). All of the prepared samples were degassed at 180 °C prior to nitrogen adsorption measurements. The BET surface area was determined by a multipoint BET method using adsorption data in the relative pressure (P/P_0) range of 0.05−0.3. A desorption isotherm was used to determine the pore size distribution via the Barret−Joyner−Halender (BJH) method, assuming a cylindrical pore model. The nitrogen adsorption volume at a relative pressure (P/P_0) of 0.972 was used to determine the pore volume and average pore size. The chemical compositions of the samples were measured by inductively coupled plasma atomic emission spectrometry (ICP−AES) using an Optima 4300 DV spectrometer (Perkin-Elmer). X-ray photoelectron spectroscopy (XPS) measurement was performed in an ultrahigh vacuum VG ESCALAB 210 electron spectrometer equipped with a multichannel detector. The spectra were excited using Mg Kα (1253.6 eV) radiation (operated at 200 W) of a twin anode in the constant analyzer energy mode with a pass energy of 30 eV. The binding energies were referenced to the C 1s line at 285.0 eV from adventitious carbon.

2.3. Computational Details. All density function theory (DFT) calculations were performed using the CASTEP Package. The Perdew−Burke−Ernzerhof (PBE) of the generalized gradient approximation (GGA) was used as the exchange-correlation function.[27,28] The ultrasoft pseudopotential was used to describe the interaction between valence electrons and ionic core. To simulate the model of the $Zn_{1-x}Cd_xS$ solid solution, we considered that the cation of the

minor component substituted the cation of the major component (i.e., the matrix). According to the XRD patterns, the cubic ZnS supercell (containing 32 Zn atoms and 32 S atoms) and the hexagonal CdS supercell (containing 32 Cd atoms and 32 S atoms) were used as the doped matrixes (see Figure 1a and b). Figure 1c shows the simulated model of
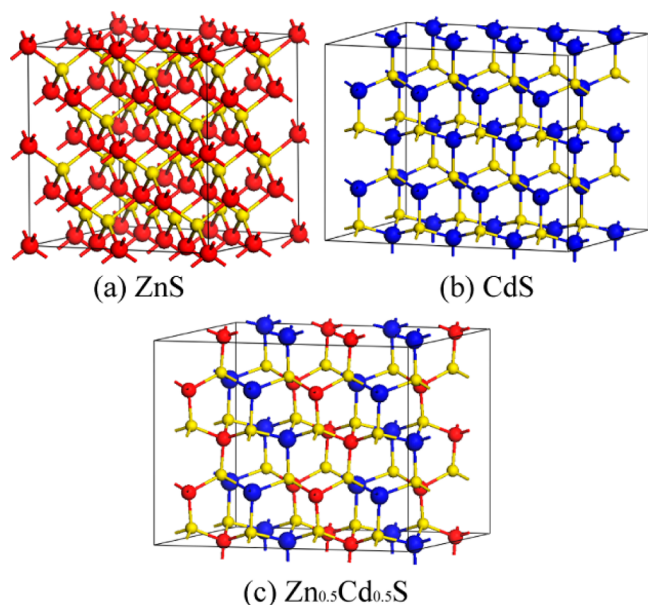

(a) ZnS   (b) CdS

(c) $Zn_{0.5}Cd_{0.5}S$

Figure 1. The supercell models for bulk (a) ZnS (64 atoms) and (b) CdS (64 atoms). The red, yellow, and blue spheres represent Zn, S, and Cd atoms, respectively. (c) The geometry model for $Zn_{0.5}Cd_{0.5}S$.

$Zn_{0.5}Cd_{0.5}S$ as one example of those $Zn_{1-x}Cd_xS$ solid solutions. The geometry optimizations were performed under the electron wave function with expansion in plane wave to a cutoff energy of 350 eV, the Monkhorst−Pack k-point mesh of $2 \times 2 \times 2$ and the self-consistent field of 5×10^{-5} eV/atom.[29] The atomic relaxations were conducted until the residual force was smaller than 0.05 eV/Å. The test calculations showed that the geometry structures of the supercells did not change significantly. Then the band structures of the supercells were calculated.

2.4. Photocatalytic Hydrogen Production. The photo-catalytic H_2 production experiments were performed in a 100 mL Pyrex flask at ambient temperature and atmospheric pressure, and the openings of the flask were sealed with silicone rubber septums. A 350 W xenon arc lamp through a UV-cutoff filter (≥400 nm), which was positioned 20 cm away from the reactor, was used as a visible light source to trigger the photocatalytic reaction. The focused intensity on the flask was ~180 mW·cm^{-2}, which was measured by a FZ-A visible-light radiometer (made in the photoelectric instrument factory of Beijing Normal University, China) with a wavelength range of 400−1000 nm. In a typical photocatalytic H_2-production experiment, 50 mg of the prepared $Zn_{1-x}Cd_xS$ photocatalyst was suspended in 80 mL of mixed aqueous solution containing Na_2S (0.44 M) and Na_2SO_3 (0.31 M) and then bubbled with nitrogen through the reactor for 30 min to completely remove the dissolved oxygen and ensure the reactor was in an anaerobic condition. A continuous magnetic stirrer was applied at the bottom of the reactor to keep the photocatalyst particles in suspension during the experiments. A 0.4 mL gas sample was intermittently sampled from the headspace of the flask through

the septum, and H_2 content was analyzed by gas chromatography (GC-14C, Shimadzu, Japan, TCD, with nitrogen as a carrier gas and 5 Å molecular sieve column). All glassware was carefully rinsed with DI water prior to use.

The apparent quantum efficiency (QE) was measured under the same photocatalytic reaction conditions, except that four 420 nm LEDs (3 W) (Shenzhen LAMPLIC Science Co. Ltd. China) were used as light sources to trigger the photocatalytic H_2-production reaction instead of the Xenon arc lamp. The LEDs were positioned 1 cm away from the reactor in four different directions, and the focused intensity on the flask for each of them was ~6.0 mW·cm^{-2} over an area of 1 cm^2. The QE was calculated according to the following equation:[30]

$$QE[\%] = \frac{\text{number of reacted electrons}}{\text{number of incident photons}} \times 100$$

$$= \frac{\text{number of evolved } H_2 \text{molecules} \times 2}{\text{number of incident photons}} \times 100$$

3. RESULTS AND DISCUSSIONS

3.1. Phase Structures and Morphology. XRD was used to investigate the crystal phase and average crystallite sizes of the prepared $Zn_{1-x}Cd_xS$ samples. Figure 2 shows the XRD

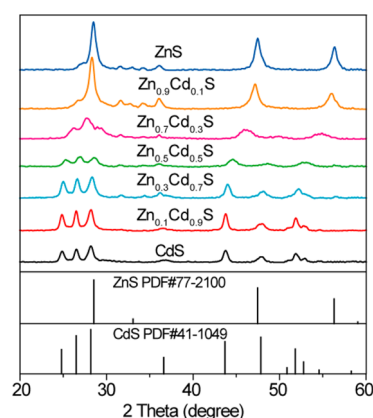**Figure 2.** XRD patterns of the $Zn_{1-x}Cd_xS$ ($x = 0$, 0.1, 0.3, 0.5, 0.7, 0.9, and 1.0) samples.

patterns of the $Zn_{1-x}Cd_xS$ ($x = 0$, 0.1, 0.3, 0.5, 0.7, 0.9, and 1.0) samples, together with the standard diffraction patterns of cubic zinc blend ZnS (JCPDS Card No. 77-2100) and hexagonal wurtzite CdS (JCPDS Card No. 41-1049). It can be seen that the diffraction peaks of the ZnS sample ($x = 0$) are well indexed as cubic ZnS. When a small amount of Cd was doped into the ZnS crystal (for the $Zn_{0.9}Cd_{0.1}S$ sample), the diffraction peaks of ZnS exhibited an obvious shift toward the lower angle. This implies that Cd^{2+} incorporates into the lattice of the ZnS crystal and increases the fringe lattice distance of the ZnS crystal due to the larger radius of Cd^{2+} (0.97 Å) than that of the Zn^{2+} ion (0.74 Å). With increasing Cd content in the $Zn_{1-x}Cd_xS$ solid solution, the XRD peak positions continuously shift to low-angle side, and the crystal phase of the $Zn_{1-x}Cd_xS$ solid solution gradually changes from the cubic to hexagonal phase and finally becomes the hexagonal wurtzite CdS phase for the CdS sample ($x = 1.0$). This implies that the Cd atoms in the ZnS crystal influence the positions of Zn atoms and consequently change the lattice structure of ZnS during the formation of the $Zn_{1-x}Cd_xS$ solid solutions under high-temperature treatment.

This phenomenon is similar to the reported results in other literatures.[17,26,31]

The average crystallite sizes of the $Zn_{1-x}Cd_xS$ samples were estimated using the Scherrer equation from the broadening of the $Zn_{1-x}Cd_xS$ (101) facet diffraction peak. As shown in Table 1, the crystallite size of the samples first decreases from 14.0 to 10.1 nm and then increases to 13.9 nm with increasing Cd content in the $Zn_{1-x}Cd_xS$ solid solution, indicating that Cd^{2+} and Zn^{2+} restrain the grain growth of pure ZnS and CdS crystals, respectively, and thus, the crystallinity of $Zn_{1-x}Cd_xS$ ($0 < x < 1$) solid solutions is worse than that of pure ZnS ($x = 0$) and CdS ($x = 1.0$).

According to the experiment, the mechanism for the formation of $Zn_{1-x}Cd_xS$ solid solution NPs is proposed. First, in the ultrasonication process (see the Experimental section), Zn^{2+} and Cd^{2+} bound to the S of thiourea to form the Zn−Cd−Tu complex due to the strong coordinating capacity of thiourea.[32−34] The formation of the Zn−Cd−Tu complex was evidenced by the XRD pattern (not shown here), which was not a simple stacking of those of the precursors (Tu, $Zn(Ac)_2·2H_2O$ and $Cd(Ac)_2·2H_2O$). The obtained Zn−Cd−Tu complex molecules aggregated to form clusters, which provided the nucleating positions for the subsequent reactions between Zn^{2+}, Cd^{2+}, and $S^{2−}$. Then, in the calcination process, the Zn−Cd−Tu complex tended to decompose and release the active Cd^{2+}, Zn^{2+} and $S^{2−}$ with increasing temperature. Consequently, these active ions reacted under high temperature and formed the $Zn_{1-x}Cd_xS$ NPs.[35] The proposed formation progress of the $Zn_{1-x}Cd_xS$ solid solution is presented in short as the following reaction:[36]

$$(1 − x)Zn^{2+} + xCd^{2+} + yTu$$
$$\rightarrow Zn_{1-x}Cd_xTu_y$$
$$\rightarrow Zn_{1-x}Cd_xS$$
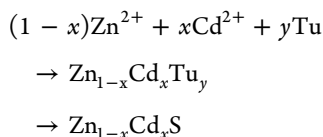
In the obtained Zn−Cd−Tu complex, thiourea not only regulated the nucleation rate of $Zn_{1-x}Cd_xS$ particles by slowly releasing $S^{2−}$ ions, but also prohibited the growth of crystals due to the pinning effect of impurity atoms, such as N and C. Thus, it is not surprising that the crystallite sizes of the prepared samples (10.1−14.0 nm) are much smaller than those generally prepared under high-temperature calcinations in the literature.[37] For photocatalytic reactions, the nanosized particles supply more surface active sites than the block particles and make charge carriers transport easier from the interior to surface of NPs, leading to an enhancement of the photocatalytic performance.

The morphologies and microstructures of the prepared samples were further characterized by TEM. The TEM micrograph in Figure 3a shows an aggregation of nanoparticles in the $Zn_{0.5}Cd_{0.5}S$ sample; the diameters of the aggregated particles are ∼50−100 nm. The HRTEM image (Figure 3b) shows that the size of the individual $Zn_{0.5}Cd_{0.5}S$ NP is about 10 nm, which is in agreement with the value calculated by the Scherrer equation (Table 1). The lattice fringes with d spacing of ∼0.31 nm can be assigned to the (101) lattice plane of the hexagonal $Zn_{0.5}Cd_{0.5}S$ (Figure 2).

3.2. UV−Visible Diffuse Reflection Spectra and Band Structure Analysis. A comparison of UV−visible diffuse absorption spectra and the corresponding colors of the $Zn_{1-x}Cd_xS$ ($x = 0$, 0.1, 0.3, 0.5, 0.7, 0.9, and 1.0) samples is displayed in Figure 4. There is an obvious and continuous red

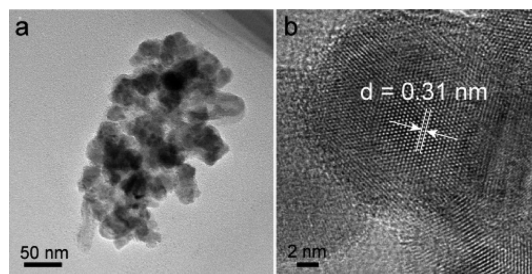**Figure 3.** (a) TEM and (b) high-resolution TEM images of the $Zn_{0.5}Cd_{0.5}S$ sample.

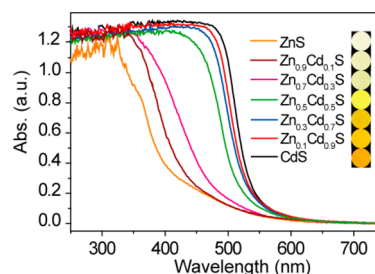**Figure 4.** UV−visible diffuse reflection spectra of the $Zn_{1-x}Cd_xS$ ($x = 0$, 0.1, 0.3, 0.5, 0.7, 0.9, and 1.0) samples.

shift of the absorption edges of the samples with increasing Cd content in $Zn_{1-x}Cd_xS$ solid solutions. This is also observed as a color change in the samples from white to yellow (inset of Figure 4). The results show that the prepared samples are not a simple mixture of ZnS and CdS, but $Zn_{1-x}Cd_xS$ solid solutions. On the other hand, the red shift of the absorption edges also implies that the band gaps of the $Zn_{1-x}Cd_xS$ solid solution photocatalysts can be precisely controlled through the thermolysis method with the variation of Zn/Cd molar ratios in precursors.

The direct band gaps of the $Zn_{1-x}Cd_xS$ samples can be determined by both experimental and theoretical methods. Experimentally, the band gaps of the $Zn_{1-x}Cd_xS$ samples were calculated according to the Kubelka−Munk (KM) method through the UV−visible diffuse absorption spectra (Figure 4) by the following equation:

$$\alpha h\nu = A(h\nu − E_g)^{1/2}$$

where α is the absorption coefficient, $h\nu$ is the photon energy, E_g is the direct band gap, and A is a constant.[38,39] The calculated band gap energy decreased from 3.10 to 2.30 eV with increasing x value from 0 to 1.0 (Table 1), indicating that the incorporated Cd atoms in the ZnS crystal narrowed its band gap and extended the absorption range of ZnS into the visible-light region. On the other hand, theoretically, the band structures of the $Zn_{1-x}Cd_xS$ samples were also calculated by DFT. As shown in Table 1, the calculated band gap energies of the samples (from 1.921 to 1.146 eV) are lower than the experimental values (from 3.10 to 2.30 eV), which is due to the well-known limitation of DFT calculation.[16] The band structure plots for the simulated $Zn_{1-x}Cd_xS$ systems can be directly observed in Figure 5. It shows that the band gap of the $Zn_{1-x}Cd_xS$ samples gradually becomes narrower from 1.921 to 1.146 eV with increasing Cd content, which is well consistent with the KM results and the UV−visible spectra (Figure 4). The narrower band gap of semiconductor photocatalyst not only benefits the absorption of more photons in sunlight, but
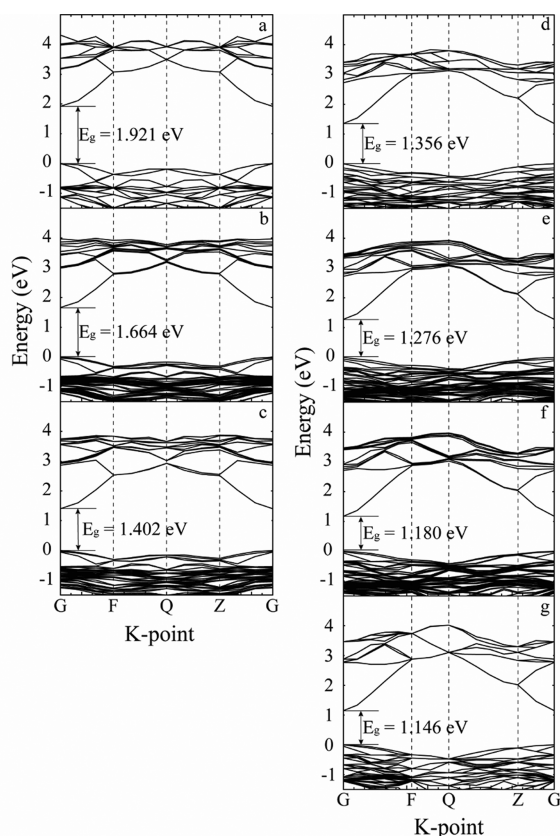
Figure 5. Band structure plots for the simulated $Zn_{1-x}Cd_xS$ systems: (a) ZnS, (b) $Zn_{0.9}Cd_{0.1}S$, (c) $Zn_{0.7}Cd_{0.3}S$, (d) $Zn_{0.5}Cd_{0.5}S$, (e) $Zn_{0.3}Cd_{0.7}S$, (f) $Zn_{0.1}Cd_{0.9}S$, (g) CdS.

Figure 6. Conduction and valence band edge potentials of the $Zn_{1-x}Cd_xS$ (x = 0, 0.1, 0.3, 0.5, 0.7, 0.9, and 1.0) samples.

dominant solid solution. However, the large band gap of the Zn-dominant solid solution is not desirable for the photocatalysis. Generally, an appropriate band gap width and suitable CB edge position together attribute to the optimal H_2-production activity under visible-light irradiation. Taking the $Zn_{0.5}Cd_{0.5}S$ sample, for example, the calculated direct band gap (2.45 eV) is narrower than that of ZnS (3.10 eV) (Table 1), and the CB energy level (−0.369 V) is more negative than that of CdS (−0.352 V) (Figure 6). Therefore, a balance between the light absorption capacity and the reduction power in the $Zn_{0.5}Cd_{0.5}S$ sample probably leads to a higher efficiency of visible-light photocatalytic H_2 production than that of the ZnS and CdS samples.

3.3. BET Surface Areas and Pore Size Distributions. Usually, photocatalysts with higher specific surface areas are beneficial for the enhancement of photocatalytic performance.[40] Thus, the BET surface areas (S_{BET}) and pore structure of the as-prepared samples were investigated by the nitrogen adsorption−desorption measurement. Figure 7 shows the

Figure 7. Nitrogen adsorption/desorption isotherms and the corresponding pore-size distribution curves (inset) of the ZnS, $Zn_{0.5}Cd_{0.5}S$ and CdS samples.

also promotes the excitation of photogenerated electrons from the valence band (VB) to the conduction band (CB), which makes the photocatalyst with visible-light H_2-production activity.

In addition to the effect of band gap width, the CB edge position of a semiconductor photocatalyst is another important factor for effective photocatalytic H_2 production. A semiconductor with a more negative CB edge level has stronger reduction power for the H_2 production from water. To determine the CB edge positions of the prepared $Zn_{1-x}Cd_xS$ semiconductors in relation to the normal hydrogen electrode potential (NHE), the following equation was employed:

$$E_{CB} = \chi - E^c - 1/2E_g$$

where E_{CB} is the CB edge potential and χ is the electronegativity of the semiconductor, expressed as the geometric mean of the absolute electronegativity of the constituent atoms. The absolute electronegativity of an individual atom is defined as the arithmetic mean of the atomic electron affinity and the first ionization energy. E^c is the energy of free electrons on the hydrogen scale, and the value is ∼4.5 eV. E_g is the direct band gap of the semiconductor, which has been calculated by the above-mentioned method.

The calculated CB and VB edge potentials of the $Zn_{1-x}Cd_xS$ samples are illustrated in Figure 6. It can be clearly seen that the CB edge potential becomes more negative with increasing Zn content (i.e., decreasing x value) in the $Zn_{1-x}Cd_xS$ solid solution, indicating that the Zn-dominant solid solution has stronger reduction power for the H_2 production than the Cd-
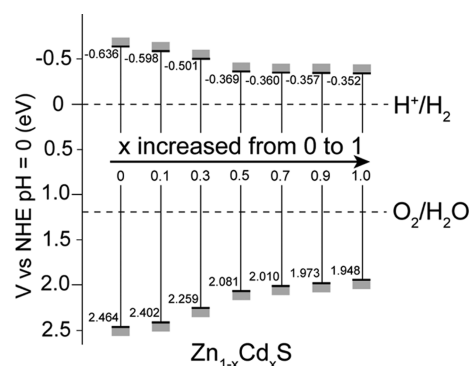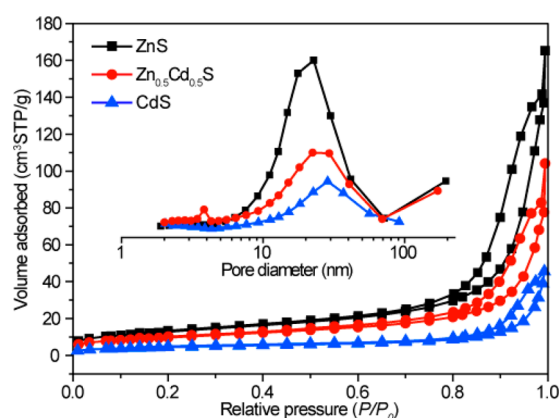
nitrogen adsorption/desorption isotherms and the corresponding pore-size distribution curves (inset) of the ZnS, $Zn_{0.5}Cd_{0.5}S$, and CdS samples. According to the Brunauer−Deming−Deming−Teller classification, the isotherms of all the samples are of type IV, indicating the presence of mesopores (2−50 nm).[41−43] Moreover, the isotherms show high adsorption at a high relative pressure (P/P_0) range from 0.8 to 1.0, suggesting the formation of large mesopores and macropores.[41] The pore

size distribution curves (inset of Figure 7) show a wide range of 2−70 nm with a peak pore diameter of ~20 nm for all the samples, further confirming the coexistence of mesopores and macropores.[44] Table 1 shows the quantitative details on the S_{BET} and average pore sizes of the $Zn_{1-x}Cd_xS$ (x = 0, 0.1, 0.3, 0.4, 0.5, 0.6, 0.7, 0.9, and 1.0) samples. The $Zn_{1-x}Cd_xS$ samples show a decreasing specific surface areas and increasing average pore sizes with increasing Cd content. The decreased specific surface areas are due to the increase in the sample density.[44] The increasing pore size is possibly from the formation of larger aggregated particles.

3.4. ICP and XPS Analysis. ICP and XPS analysis were explored to gain deeper insight into the bulk and surface compositions of the prepared $Zn_{1-x}Cd_xS$ samples. Figure 8a
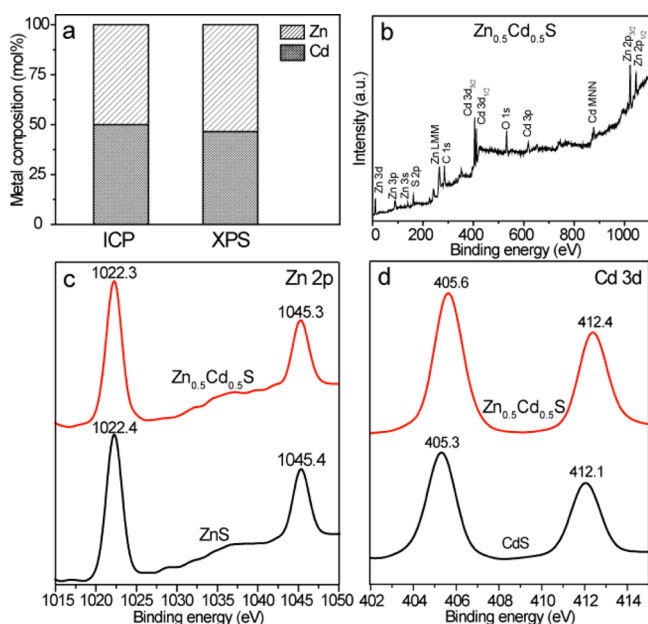

Figure 8. (a) The bulk and surface metal compositions of the $Zn_{0.5}Cd_{0.5}S$ sample measured by ICP (left) and XPS (right) methods, respectively; (b) XPS survey spectrum of the $Zn_{0.5}Cd_{0.5}S$ sample; (c) Zn 2p XPS spectra of the ZnS (bottom) and $Zn_{0.5}Cd_{0.5}S$ (top) samples; (d) Cd 3d XPS spectra of the CdS (bottom) and $Zn_{0.5}Cd_{0.5}S$ (top) samples.

compares the metal compositions of the $Zn_{0.5}Cd_{0.5}S$ sample measured by ICP and XPS methods, respectively. In the ICP result, the Zn/Cd ratio is 50:50, whereas in the XPS result, the Zn/Cd ratio is 53.6:46.4. Both of them are close to the stoichiometric ratio of Zn and Cd in the initial solution. ICP results of other samples are presented in Table 1, which shows that the final Zn/Cd molar ratios of all the prepared $Zn_{1-x}Cd_xS$ solid solutions are almost the same with the initial ones, which is difficult to achieve by some other methods, such as hydrothermal and coprecipitation.[15,17]

Figure 8b presents the survey spectrum of the $Zn_{0.5}Cd_{0.5}S$ sample, which confirms the coexistence of Zn, Cd, and S elements as expected. The positions of S $2p_{1/2}$ and S $2p_{3/2}$ high-resolution XPS signals for the $Zn_{0.5}Cd_{0.5}S$ sample are around 163.0 and 161.8 eV, respectively, which are the same with the values of S in pure ZnS and CdS (not shown here). The XPS spectra of Zn 2p and Cd 3d are plotted in Figure 8c and d, respectively. For the ZnS and CdS samples, the binding energies of Zn 2p and Cd 3d agree well with the values

reported for the divalent zinc and cadmium in pure metal sulphides, respectively;[45−47] however, for the $Zn_{0.5}Cd_{0.5}S$ sample, the peak positions of Zn 2p shifted to lower values by 0.1 eV, and those of Cd 3d shifted to higher values by 0.3 eV compared with that of the ZnS and CdS samples, respectively, which was also presented in other work.[46] This is due to the changed chemical states of the Zn and Cd atoms in the $Zn_{0.5}Cd_{0.5}S$ sample.

To investigate the cause of the chemical shifts of Zn, Cd and S atoms in the $Zn_{0.5}Cd_{0.5}S$ sample, the Mulliken populations of Zn, Cd and S atoms in the stimulated ZnS, CdS and $Zn_{0.5}Cd_{0.5}S$ (Figure 1) are calculated. The result is displayed in Table 2. Generally, the Mulliken populations of metal atom

Table 2. The Mulliken Populations of Zn, Cd and S Atoms in ZnS, CdS and $Zn_{0.5}Cd_{0.5}S$

model	Zn	Cd	S
ZnS	0.48		−0.48
CdS		0.60	−0.60
$Zn_{0.5}Cd_{0.5}S$	0.51	0.58	−0.54

and S atom are the same in pure metal sulfide. For example, in pure ZnS and CdS, the Mulliken populations of Zn and Cd atoms are 0.48 and 0.60, respectively. In contrast, that of the S atom for ZnS and CdS is −0.48 and −0.60, respectively. The difference in the Mulliken populations of Zn and Cd atoms derives from the larger first ionization energy of Zn atom than that of the Cd atom. On the other hand, in the $Zn_{0.5}Cd_{0.5}S$ sample, the Mulliken population of the S atom is −0.54, which is just half of the sum for pure ZnS and CdS. This implies that the chemical status (or binding energy) of the S atom in the $Zn_{0.5}Cd_{0.5}S$ sample has no obvious change. This also is in agreement with the XPS results of the S atom. However, the Mulliken population of Zn atom (0.51) is lower than that of the S atom (−0.54), but the Mulliken population of Cd atoms (0.58) is higher than that of the S atom (−0.54), indicating that the Zn atom loses fewer electrons and the Cd atom loses more electrons in $Zn_{0.5}Cd_{0.5}S$ solid solution compared with that in pure ZnS and CdS, respectively. This is also caused by the difference in the first ionization energy of Zn and Cd atoms. Therefore, the redistribution of charges between Zn and Cd atoms in the $Zn_{0.5}Cd_{0.5}S$ sample leads to the chemical shifts in the XPS spectra (Figure 8c and d). The XPS result and the calculated Mulliken populations further confirmed the formation of the $Zn_{1-x}Cd_xS$ solid solutions.

3.5. Photocatalytic Activity. The applicability of chalcogenide nanomaterials has been widely explored for H_2 production from water splitting under visible-light irradiation. For example, Bao et al. synthesized CdS nanocrystals through a Cd−thiourea complex thermolysis method.[25] The sample synthesized under similar situation with our work has a visible-light photocatalytic H_2 production rate of 0.90 mmol·h^{-1}·g^{-1} with 3 wt % Pt as the cocatalyst; however, a $Zn_{1-x}Cd_xS$ solid solution usually exhibits a higher H_2-production activity than CdS alone.[15,17,48] And it is noteworthy that avoiding the usage of noble metals as the cocatalyst is highly valued from a practical point of view for the application of photocatalytic H_2-production techniques.[13,22] For example, Guo et al. synthesized $Zn_{1-x}Cd_xS$ solid solution through a coprecipitation method followed by heat treatment.[17] Among the prepared samples, CdS showed a negligible photocatalytic activity and $Zn_{0.16}Cd_{0.62}S$ showed high photocatalytic activity

with a H_2-production rate of 0.67 mmol·h^{-1}·g^{-1} under visible-light irradiation without noble metal as a cocatalyst. Wang et al. used sodium dodecylsulfate (SDS) as the surfactant and synthesized $Zn_{1-x}Cd_xS$ solid solution.[15] The visible-light photocatalytic H_2-production rate of the $Zn_{0.56}Cd_{0.44}S$ sample was as high as 2.64 mmol·h^{-1}·g^{-1}. In this work, photocatalytic H_2-production activities of the prepared $Zn_{1-x}Cd_xS$ solid solutions were evaluated under visible-light irradiation using Na_2S and Na_2SO_3 mixed aqueous solution as the sacrificial reagent without noble metals as cocatalyst. It was expected that higher photocatalytic H_2-production efficiency could be achieved for the $Zn_{1-x}Cd_xS$ photocatalysts prepared through the Zn−Cd−Tu complex thermolysis method.

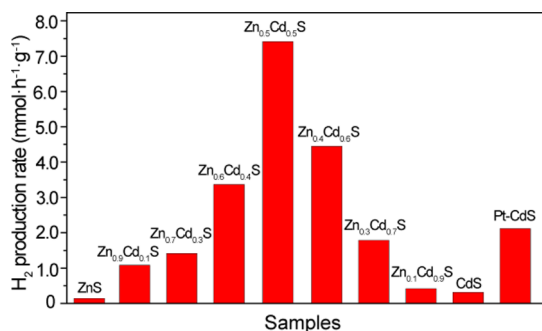Figure 9 presents the comparison of the visible-light photocatalytic H_2-production rates of the $Zn_{1-x}Cd_xS$ ($x = 0$,

Figure 9. Comparison of the photocatalytic activities of the $Zn_{1-x}Cd_xS$ ($x = 0$, 0.1, 0.3, 0.4, 0.5, 0.6, 0.7, 0.9, and 1.0) samples for the photocatalytic H_2-production from 0.44 M Na_2S and 0.31 M Na_2SO_3 mixed aqueous solution under visible-light ($\geq$400 nm) irradiation. The photocatalytic activity of 0.9 wt % Pt loaded CdS (Pt−CdS) under the same condition was also performed to make comparison.

0.1, 0.3, 0.4, 0.5, 0.6, 0.7, 0.9, and 1.0) samples. The pure ZnS ($x = 0$) shows a negligible visible-light photocatalytic activity with a H_2-production rate of 0.14 mmol·h^{-1}·g^{-1}. As the Cd content increases, the H_2-production rate of $Zn_{1-x}Cd_xS$ becomes higher and up to 7.42 mmol·h^{-1}·g^{-1} when the nominal x value is 0.5 (for the $Zn_{0.5}Cd_{0.5}S$ sample), exceeding that of pure ZnS by more than 54 times, and even much higher than that of an optimal Pt (0.9 wt %) loaded CdS (Pt−CdS) photocatalyst (4.70 mmol·h^{-1}·g^{-1}). The corresponding apparent QE at 420 nm reaches 9.6% for the $Zn_{0.5}Cd_{0.5}S$ sample; however, a further increase in the Cd content in the $Zn_{1-x}Cd_xS$ solid solution led to a fast deterioration of the photocatalytic performance. Especially, the pure CdS ($x = 1.0$) shows a low activity with a H_2-production rate of only 0.31 mmol·h^{-1}·g^{-1} in the absence of a cocatalyst. After taking the specific surface area into consideration, the H_2-production rates per unit area of the samples still follow the same ranking (not shown here). Thus, it can be confirmed that the change in surface area of $Zn_{1-x}Cd_xS$ solid solutions was not a crucial factor leading to greatly improved photoactivity, and the light-absorption capability and the CB edge position of the $Zn_{1-x}Cd_xS$ solid solutions are more significant factors influencing the H_2-production photoactivity. Typically, as analyzed in Figure 6, the ZnS ($x = 0$) sample has a prominent ability of H^+ reduction but cannot absorb visible light because of its large band gap, whereas the CdS ($x = 1.0$) sample has a proper band gap width to utilize visible light but is weak for H_2 production because of its low position of the CB edge. For the $Zn_{0.5}Cd_{0.5}S$ sample, the balance between two

factors of light-absorption capacity and CB potential makes it with the highest H_2-production efficiency.

On the other hand, the fabrication method also affects the photocatalytic activity of H_2 production. Especially, the $Zn_{1-x}Cd_xS$ solid solutions prepared by the Zn−Cd−Tu complex thermolysis method have much better activities than that prepared by some other methods, such as hydrothermal and coprecipitation.[15,17] This is attributed to the following reasons: (1) The ultrasonication treatment makes the precursors mix well and react completely to form the Zn−Cd−Tu complex. (2) There is no loss of precursors during the whole fabrication process; thus, the Zn and Cd contents in the $Zn_{1-x}Cd_xS$ solid solutions remain almost unchanged, and the fabrication of the ternary solid solution can be precisely controlled. (3) Thiourea as the S resource not only slowly releases S^{2-} ions, but also supplies impurity atoms (N and C) as the pinning points in the Zn−Cd−Tu complex, which results in the small crystallite size of $Zn_{1-x}Cd_xS$ particles and thus improves the photocatalytic activity. Thus, the Zn−Cd−Tu complex thermolysis is confirmed to be an effect method to produce highly efficient $Zn_{1-x}Cd_xS$ solid solution photocatalysts for H_2 production from water.

4. CONCLUSIONS

In summary, a simple zinc−cadmium−thiourea complex thermolysis method has been successfully developed to fabricate highly visible-light active $Zn_{1-x}Cd_xS$ solid solutions for photocatalytic H_2 production. The final metal concentration in the prepared $Zn_{1-x}Cd_xS$ samples is nearly the same with the initial one in the precursor. When the Zn/Cd molar ratio is 1:1, the $Zn_{0.5}Cd_{0.5}S$ sample without any cocatalyst exhibits the optimal H_2-production rate of 7.42 mmol·h^{-1}·g^{-1} with a QE of 9.6% at 420 nm, which is even much higher than that of the optimal Pt-loaded CdS. The aforementioned high rate value is attributed to the balance between the band gap width and CB edge position of the $Zn_{0.5}Cd_{0.5}S$ sample. The result is further proven by the theory calculation on the band structures of the $Zn_{1-x}Cd_xS$ solid solutions. Moreover, the calculation on the Mulliken populations of Zn, Cd, and S atoms confirms that the charge redistribution between Zn and Cd atoms in the $Zn_{1-x}Cd_xS$ samples leads to the chemical shifts of element binding energies for the $Zn_{1-x}Cd_xS$ solid solutions, which is helpful for designing other new ternary photocatalytic materials. This work not only demonstrates a facile and new method to produce highly active $Zn_{1-x}Cd_xS$ materials for H_2 production from water splitting, but also provides new insights into understanding the mechanism of visible-light absorption and photoactive enhancement for $Zn_{1-x}Cd_xS$ solid solution.

■ AUTHOR INFORMATION

Corresponding Author
*E-mails: (J.Y.) jiaguoyu@yahoo.com, (J.R.G.)) gongjr@nanoctr.cn.

Notes
The authors declare no competing financial interest.

■ ACKNOWLEDGMENTS

■ REFERENCES

(1) Cortright, R. D.; Davda, R. R.; Dumesic, J. A. *Nature* **2002**, *418*, 964−967.

(2) (a) Yu, J. G.; Ran, J. R. *Energy Environ. Sci.* **2011**, *4*, 1364−1371. (b) Xiang, Q. J.; Yu, J. G. *J. Phys. Chem. Lett.* **2013**, *4*, 753−759.

(3) Fujishima, A.; Honda, K. *Nature* **1972**, *238*, 37−38.

(4) Xiang, Q. J.; Yu, J. G.; Jaroniec, M. *J. Am. Chem. Soc.* **2012**, *134*, 6575−6578.

(5) Park, J. H.; Kim, S.; Bard, A. J. *Nano Lett.* **2006**, *6*, 24−28.

(6) (a) Hoffmann, M. R.; Martin, S. T.; Choi, W.; Bahnemann, D. W. *Chem. Rev.* **1995**, *95*, 69−96. (b) Xiang, Q. J.; Yu, J. G.; Jaroniec, M. *Chem. Soc. Rev.* **2012**, *41*, 782−796.

(7) Zou, Z. G.; Ye, J. H.; Sayama, K.; Arakawa, H. *Nature* **2001**, *414*, 625−627.

(8) Li, Q.; Guo, B. D.; Yu, J. G.; Ran, J. R.; Zhang, B. H.; Yan, H. J.; Gong, J. R. *J. Am. Chem. Soc.* **2011**, *133*, 10878−10884.

(9) Ran, J. R.; Yu, J. G.; Jaroniec, M. *Green Chem.* **2011**, *13*, 2708−2713.

(10) (a) Yu, J. G.; Dai, G. P.; Huang, B. B. *J. Phys. Chem. C* **2009**, *113*, 16394−16401. (b) Xiang, Q. J.; Yu, J. G.; Wang, W. G.; Jaroniec, M. *Chem. Commun.* **2011**, *47*, 6906−6908. (c) Xiang, Q. J.; Yu, J. G.; Jaroniec, M. *Nanoscale* **2011**, *3*, 3670−3678.

(11) (a) Reber, J. F.; Rusek, M. *J. Phys. Chem.* **1986**, *90*, 824−834. (b) Zhang, J.; Yu, J. G.; Zhang, Y. M.; Li, Q.; Gong, J. R. *Nano Lett.* **2011**, *11*, 4774−4779. (c) Zhang, J.; Liu, S. W.; Yu, J. G.; Jaroniec, M. *J. Mater. Chem.* **2011**, *21*, 14655−14662. (d) Zhang, J.; Yu, J. G.; Jaroniec, M.; Gong, J. R. *Nano Lett.* **2012**, *12*, 4584−4589.

(12) (a) Matsumura, M.; Furukawa, S.; Saho, Y.; Tsubomura, H. *J. Phys. Chem.* **1985**, *89*, 1327−1330. (b) Yu, J. G.; Yu, Y. F.; Cheng, B. *RSC Adv.* **2012**, *2*, 11829−11835. (c) Xiang, Q. J.; Cheng, B.; Yu, J. G. *Appl. Catal., B* **2013**, *138−139*, 299−303.

(13) Yu, J. G.; Zhang, J.; Jaroniec, M. *Green Chem.* **2010**, *12*, 1611−1614.

(14) Yu, X. X.; Yu, J. G.; Cheng, B.; Huang, B. B. *Chem.—Eur. J.* **2009**, *15*, 6731−6739.

(15) Wang, L.; Wang, W. Z.; Shang, M.; Yin, W. Z.; Sun, S. M.; Zhang, L. *Int. J. Hydrogen Energy* **2010**, *35*, 19−25.

(16) Wu, J. C.; Zheng, J.; Zacherl, C. L.; Wu, P.; Liu, Z. K.; Xu, R. *J. Phys. Chem. C* **2011**, *115*, 19741−19748.

(17) Xing, C. J.; Zhang, Y. J.; Yan, W.; Guo, L. J. *Int. J. Hydrogen Energy* **2006**, *31*, 2018−2024.

(18) Del Valle, F.; Ishikawa, A.; Domen, K.; Villoria de La Mano, J.; Sánchez-Sánchez, M.; González, I.; Herreras, S.; Mota, N.; Rivas, M.; Álvarez Galván, M. *Catal. Today* **2009**, *143*, 51−56.

(19) Chen, D. L.; Gao, L. *Solid State Commun.* **2005**, *133*, 145−150.

(20) Al Kuhaimi, S.; Tulbah, Z. *J. Electrochem. Soc.* **2000**, *147*, 214−218.

(21) Nie, Q. L.; Yuan, Q. L.; Wang, Q. S.; Xu, Z. D. *J. Mater. Sci.* **2004**, *39*, 5611−5612.

(22) Yu, J. G.; Yang, B.; Cheng, B. *Nanoscale* **2012**, *4*, 2670−2677.

(23) Sung, Y. M.; Lee, Y. J.; Park, K. S. *J. Am. Chem. Soc.* **2006**, *128*, 9002−9003.

(24) Wang, X.; Liu, G.; Chen, Z. G.; Li, F.; Lu, G. Q.; Cheng, H. M. *Electrochem. Commun.* **2009**, *11*, 1174−1178.

(25) Bao, N. Z.; Shen, L. M.; Takata, T.; Domen, K.; Gupta, A.; Yanagisawa, K.; Grimes, C. A. *J. Phys. Chem. C* **2007**, *111*, 17527−17534.

(26) Naumov, A.; Samofalova, T.; Semenov, V.; Nechaev, I. *Russ. J. Inorg. Chem.* **2011**, *56*, 621−627.

(27) Perdew, J. P.; Burke, K.; Ernzerhof, M. *Phys. Rev. Lett.* **1996**, *77*, 3865−3868.

(28) Perdew, J. P.; Wang, Y. *Phys. Rev. B* **1992**, *45*, 13244−13249.

(29) Monkhorst, H. J.; Pack, J. D. *Phys. Rev. B* **1976**, *13*, 5188−5192.

(30) Yu, J. G.; Hai, Y.; Cheng, B. *J. Phys. Chem. C* **2011**, *115*, 4953−4958.

(31) Zhang, K.; Jing, D. W.; Xing, C. J.; Guo, L. J. *Int. J. Hydrogen Energy* **2007**, *32*, 4685−4691.

(32) Semenov, V.; Averbakh, E.; Mikhaleva, L. *Zh. Neorg. Khim.* **1979**, *24*, 911−915.

(33) Krunks, M.; Mellikov, E. Y.; Sork, E. *Zh. Neorg. Khim.* **1985**, *30*, 1373−1376.

(34) Naumov, A.; Nechaev, I.; Samofalova, T.; Semenov, V. *Russ. J. Appl. Chem.* **2010**, *83*, 974−977.

(35) Naumov, A. V.; Semenov, V. N.; Bolgova, T. G.; Sergeeva, A. V. *Vestn. Voronezh. Gos. Univ. Ser. Khim. Biol.* **2005**, *1*, 6−68.

(36) Sreejith, K.; Mali, K.; Pillai, C. *Mater. Lett.* **2008**, *62*, 95−99.

(37) Jing, D. W.; Guo, L. J. *J. Phys. Chem. B* **2006**, *110*, 11139−11145.

(38) Serpone, N.; Lawless, D.; Khairutdinov, R. *J. Phys. Chem.* **1995**, *99*, 16646−16654.

(39) Patterson, E.; Shelden, C.; Stockton, B. *Appl. Opt.* **1977**, *16*, 729−732.

(40) Ishibashi, K.; Fujishima, A.; Watanabe, T.; Hashimoto, K. *Electrochem. Commun.* **2000**, *2*, 207−210.

(41) Sing, K. S.; Everett, D. H.; Haul, R.; Moscou, L.; Peirotti, R. A.; Rouquerol, J.; Siemieniewska, T. *Pure Appl. Chem.* **1982**, *54*, 2201−2218.

(42) Pierotti, R.; Rouquerol, J. *Pure Appl. Chem.* **1985**, *57*, 603−619.

(43) Kruk, M.; Jaroniec, M. *Chem. Mater.* **2001**, *13*, 3169−3183.

(44) Yu, J. G.; Qi, L. F.; Jaroniec, M. *J. Phys. Chem. C* **2010**, *114*, 13118−13125.

(45) Tejos, R. M.; Rolon, B. G.; Del, R. R.; Cabello, G. *J. Chil. Chem. Soc.* **2007**, *52*, 1257−1260.

(46) Fan, C. C.; Wang, X. T.; Sang, H. X.; Wang, F. *Int. J. Photoenergy* **2012**, Article ID 492746.

(47) Qi, L. F.; Yu, J. G.; Jaroniec, M. *Phys. Chem. Chem. Phys.* **2011**, *13*, 8915−8923.

(48) Zhang, K.; Jing, D. W.; Chen, Q. Y.; Guo, L. J. *Int. J. Hydrogen Energy* **2010**, *35*, 2048−2057.